

# Registered and antiregistered phase separation of mixed amphiphilic bilayers (condensed title: ‘Bilayer registration/antiregistration’)

J. J. Williamson<sup>1,2,\*</sup> and P. D. Olmsted<sup>1,2,†</sup>

<sup>1</sup>*Department of Physics, Institute for Soft Matter Synthesis and Metrology, Georgetown University, 37th and O Streets, N.W., Washington, D.C. 20057, USA*

<sup>2</sup>*Soft Matter Physics Group, School of Physics and Astronomy, University of Leeds, Leeds LS2 9JT, UK*

(Dated: March 28, 2022)

## Abstract

We derive a mean-field free energy for phase separation in coupled bilayer leaflets, physics which is central to myriad cellular processes and to the design of artificial membranes. Our model accounts for amphiphile-level structure, in particular hydrophobic mismatch, which promotes *antiregistration* (AR), in competition with the ‘direct’ trans-midplane coupling usually studied, promoting registration (R). For phospholipid parameters, equilibrium demixing is typically R, but hydrophobic mismatch favours metastable AR phases, which can cause a bilayer in the ‘spinodal region’ to require nucleation in order to equilibrate. This provides a framework for understanding disparate existing observations, elucidating a subtle, often overlooked competition of couplings, and a key role for phase transition kinetics in determining domain registration/antiregistration.

Keywords: Membranes, Rafts, Inter-leaflet coupling, Domains, Free energy, Coarse-graining

---

\* johnjosephwilliamson@gmail.com; Current address: Department of Physics, Institute for Soft Matter Synthesis and Metrology, Georgetown University, 37th and O Streets, N.W., Washington, D.C. 20057, USA

† pdo7@georgetown.edu; Permanent address: Department of Physics, Institute for Soft Matter Synthesis and Metrology, Georgetown University, 37th and O Streets, N.W., Washington, D.C. 20057, USA

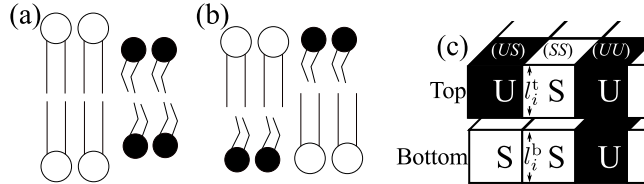


FIG. 1. (a) Registration (R), satisfying the direct coupling but with thickness mismatch penalised by the indirect coupling. (b) Antiregistration (AR), without thickness variation but a mismatch penalty from the direct coupling. (c) Lattice model for coupled bilayer leaflets.

## I. INTRODUCTION

Phase separation in amphiphilic bilayers is of great interest due to cellular roles of lipid ‘rafts’ (1, 2), and as a means of designing function into artificial membranes. A full understanding of their rich phase behaviour requires consideration of the separate, yet coupled, leaflets of the bilayer (3–9). Such inter-leaflet coupling is especially important in, e.g., mechanisms of protein localisation via domain formation (2).

Experiment and simulation yield disparate results. Observations of registered domains (10) (Fig. 1a) imply a mismatch free energy per area favouring registration (R), which we call ‘direct’ coupling (11). However, R domains typically differ in hydrophobic thickness,  $\sim 1$  nm for liquid-ordered vs. liquid-disordered (LO-LD) phospholipid domains, leading to energetically costly hydrophobic mismatch. Thus an ‘indirect’ coupling promotes *antiregistration* (AR) to relieve thickness mismatch (Fig. 1b), in competition with the direct coupling. Antiregistration was inferred experimentally at the single-amphiphile level (12), while AR *domains* have appeared in LO-LD (13) and liquid-gel (14) simulations, and AFM has shown R domains decaying into AR (15).

Despite its wide practical importance, this complex behaviour lacks a full theoretical picture. Existing theories (3, 7) treat the bilayer as two phenomenologically coupled phase-separating leaflets, with an order parameter to describe the demixing transition. The phenomenological parameters in these models are not directly related to molecular features of bilayers. Hydrophobic mismatch is often not explicitly included in coarse-grained modelling (3, 5, 7, 9, 16), so that the competition of direct and indirect inter-leaflet couplings described above cannot be captured (17).

We approach the problem using a mean-field free energy derived from a lattice model of coupled leaflets, in which simplified molecular interactions and bilayer structuring, including hydrophobic mismatch, appear explicitly. We show how competing interactions (favouring Fig. 1a, 1b) lead to rich free energy landscapes, thereby unifying observations of registration and antiregistration (10, 13–15). We point out the importance of *kinetics*, showing how a bilayer can be influenced by metastable antiregistered phases. As a consequence, a bilayer in the conventional ‘spinodal’ region can, paradoxically, require nucleation in order to equilibrate.

## II. THEORY

### A. Lattice bilayer model

To obtain the mean-field free energy, we begin with a lattice model (Fig. 1c) for the two leaflets and their competing direct and indirect couplings. A patch of the bilayer is modelled as an  $L^2 = N$  square lattice of sites, where each site contains a ‘top’ (t) and ‘bottom’ (b) leaflet amphiphile. The lattice spacing is the lateral distance between amphiphiles,  $a \sim 0.8$  nm for phospholipids. Each amphiphile has a hydrophobic length  $\ell_i^{t(b)}$ . We define the bilayer thickness  $d_i \equiv \ell_i^t + \ell_i^b$ , and the difference  $\Delta_i \equiv \ell_i^t - \ell_i^b$ . Extension of the tails also entails greater ordering, which we implicitly map onto the length variables  $\ell_i^{t(b)}$  (18). We define  $\hat{\phi}_i^{t(b)} = 1$  or 0 if the top (bottom) of site  $i$  contains an ‘S’ or ‘U’ species amphiphile. These labels are chosen to suggest saturated and unsaturated lipids, where  $S$  prefers a longer, more ordered tail structure; however they can represent any two species, or phases of a ternary ( $S + U +$  cholesterol) bilayer on a two phase tie-line (16, 19, 20). Each lattice site may be ‘pairwise’ registered ( $SS$  or  $UU$ ), or antiregistered ( $SU$  or  $US$ ). The species-dependent ideal hydrophobic lengths are  $\ell_{S0}$ ,  $\ell_{U0}$ . We define  $\Delta_0 \equiv \ell_{S0} - \ell_{U0}$ ,  $d_0 \equiv \ell_{S0} + \ell_{U0}$ . We choose  $\ell_{S0} > \ell_{U0}$ , although this choice is arbitrary.

The exact lattice Hamiltonian considered is

$$H = \sum_{\langle i,j \rangle} (V_{\hat{\phi}_i^t \hat{\phi}_j^t} + V_{\hat{\phi}_i^b \hat{\phi}_j^b}) + \sum_{\langle i,j \rangle} \frac{1}{2} \tilde{J} (d_i - d_j)^2 + \sum_i \frac{1}{2} B (\Delta_i)^2 + \sum_i \frac{1}{2} \kappa ((\ell_i^t - \ell_0^t)^2 + (\ell_i^b - \ell_0^b)^2) , \quad (1)$$

where  $\ell_0^{t(b)i} = \ell_{S0}$  for an  $S$  amphiphile at the top (bottom) of site  $i$ , or  $\ell_{U0}$  for  $U$ .

The first two terms of  $H$  are nearest-neighbour interactions. An Ising interaction  $V_{\dots}$  occurs among  $S$  and  $U$  amphiphiles within each leaflet separately, representing interactions independent of amphiphile length, such as those between headgroups. The hydrophobic penalty  $\tilde{J}$  acts on the *total* bilayer thickness, ‘indirectly’ coupling the top and bottom amphiphiles of a given site via the surrounding thickness, and favours antiregistration to minimise thickness variation (Fig. 1b). The final two terms are on-site terms;  $B$  is a direct coupling that favours registration (R), similarly to the conventional mismatch free energy density  $\gamma$  (3, 4, 21, 22), by penalising differences in length (thus tail ordering) between the top and bottom amphiphiles of a site.  $\kappa$  penalises length stretching relative to the species’ ideal lengths.

### B. Coarse-grained free energy

Our goal is the free energy per site  $f$ , as a function only of coarse-grained (i.e. locally averaged) variables for the composition  $\bar{\phi}^{t(b)} \equiv N_S^{t(b)}/N$  and thickness of each leaflet. We calculate this within a mean-field approximation (detailed in Appendix A) in which the neighbour terms of Eq. 1 involving  $V$  and  $\tilde{J}$  are approximated by on-site terms. The coarse-

grained variables impose constraints

$$\sum_{\alpha} N_{\alpha} d_{\alpha} = N \bar{d} , \quad (2a)$$

$$\sum_{\alpha} N_{\alpha} \Delta_{\alpha} = N \bar{\Delta} , \quad (2b)$$

$$N_{SU} - N_{US} = (\bar{\phi}^t - \bar{\phi}^b) N , \quad (2c)$$

$$N_{SS} + N_{SU} = \bar{\phi}^t N , \quad (2d)$$

$$N_{UU} + N_{US} = (1 - \bar{\phi}^t) N , \quad (2e)$$

where  $N_{\alpha}$  are the occupancies of the four possible site types  $\alpha \in \{SS, UU, SU, US\}$  with thickness variables  $d_{\alpha}, \Delta_{\alpha}$ . We find that the desired mean-field free energy  $f(\bar{\phi}^t, \bar{\phi}^b, \bar{d}, \bar{\Delta})$  is given by minimising

$$f' N = \sum_{\alpha} (N_{\alpha} H_{\alpha} + k_B T N_{\alpha} \ln N_{\alpha}) - 2VN(\bar{\phi}^t - \bar{\phi}^b)^2 - 2VN(\bar{\phi}^t + \bar{\phi}^b - 1)^2 , \quad (3)$$

subject to Eqs. 2a–2e, where  $H_{\alpha}$  contain the thickness-dependent, mean-field interactions for each site type

$$H_{\alpha} = \frac{1}{2} J (d_{\alpha} - \bar{d})^2 + \frac{1}{2} B (\Delta_{\alpha})^2 + \frac{1}{2} \kappa ((\ell_{\alpha}^t - \ell_0^{t\alpha})^2 + (\ell_{\alpha}^b - \ell_0^{b\alpha})^2) , \quad (4)$$

in which  $\ell_0^{t\alpha} = \ell_{A0}$ ,  $\ell_0^{b\alpha} = \ell_{B0}$  for  $\alpha = AB$ , and  $J \equiv 4\tilde{J}$ .  $V \equiv V_{10} - \frac{1}{2}(V_{11} + V_{00})$  sets the strength of the length-independent interaction.

$f$  may further be minimised over the coarse-grained total thickness  $\bar{d}$  and thickness difference  $\bar{\Delta}$  to yield their annealed values  $\bar{d}^{[\text{ann.}]} = \Delta_0(\bar{\phi}^t + \bar{\phi}^b - 1) + d_0$  and  $\bar{\Delta}^{[\text{ann.}]} = \kappa \Delta_0(\bar{\phi}^t - \bar{\phi}^b)/(2B + \kappa)$ . The bilayer's phase behaviour is governed by

$$f^{[\text{ann.}]}(\bar{\phi}^t, \bar{\phi}^b) \equiv f(\bar{\phi}^t, \bar{\phi}^b, \bar{d}^{[\text{ann.}]}, \bar{\Delta}^{[\text{ann.}]}) . \quad (5)$$

Because the free energy is explicitly symmetric under species interchange, tie-line endpoints ‘1’ and ‘2’ in the individual leaflets satisfy  $\bar{\phi}_1^{t(b)} = 1 - \bar{\phi}_2^{t(b)}$  (this symmetry does not imply a loss of generality in the qualitative findings). Local demixing of the bilayer can be R,  $\bar{\phi}_R^b(\bar{\phi}^t) = \bar{\phi}^t$  or AR,  $\bar{\phi}_{AR}^b(\bar{\phi}^t) = 1 - \bar{\phi}^t$ , which respectively entail a local preponderance of *pairwise* R or AR amphiphile pairs.

### III. RESULTS

We now study particular details of the free energy derived from our model, after first discussing the estimated parameters used. Then, we combine these separate analyses in Section III E (Fig. 4).

#### A. Parameter choices

The length-independent Ising interaction strength  $V$  controls whether the leaflets would demix in the *absence* of coupling ( $J = B = 0$ , such that each leaflet acts as an independent

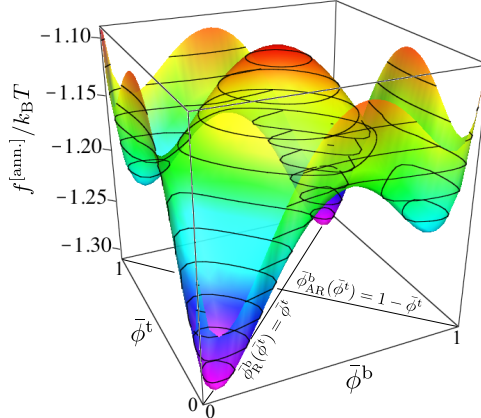


FIG. 2. Free energy as a function of top and bottom leaflet compositions for the state point marked in Fig. 4c.

Ising lattice). In the MF approximation, the Ising model requires  $V > V_0 \equiv 0.5 k_B T$  to demix, so we test values of  $V$  above and below this threshold in the present work. The indirect coupling  $\tilde{J}$  quantifies the penalty for mismatched total hydrophobic thickness, arising from hydrophobic surface tension. We take a fiducial value  $\tilde{J} \approx 0.8 k_B T \text{nm}^{-2}$ , estimated in Ref. (23) as a surface tension for hydrocarbon tails in contact with the watery headgroups of phospholipids. This gives  $\tilde{J} \approx 0.5 a^{-2} k_B T$ , thus  $J \approx 2 a^{-2} k_B T$ ; varying  $J$  about this value can be thought of as varying the strength of hydrophobic mismatch/hydrophobicity. The direct coupling parameter  $B$  plays a similar role to the inter-leaflet mismatch energy  $\gamma$ , for which widely varying estimates have been made. We define effective values of  $\gamma$  from our choices of  $B$ , which are plotted on Fig. 4 for reference. Details of this mapping, and the subtleties of defining and measuring inter-leaflet coupling, are given in Appendix C. Finally, the stretching modulus  $\kappa$  can be related to the *area* stretching modulus  $\kappa_A$  (see Appendix C) – we use a value of  $\kappa$  corresponding to  $\kappa_A \approx 60 k_B T \text{nm}^{-2}$ .

## B. Free energy landscapes

An example free energy landscape is shown in Fig. 2. For this state point (marked in Fig. 4c), both R and AR demixed minima exist, with R being the equilibrium (lowest free energy) phases. The presence of metastable minima implies nontrivial *kinetics* for registration and antiregistration (similarly, metastable gas-liquid coexistence can cause complex kinetics in the freezing transition of colloids (24)). Consider, for example, the kinetics of an initial ‘mixed state’ ( $\bar{\phi}^b = \bar{\phi}^t = 0.5$ ), as would exist after quenching a bilayer with an equimolar mixture in each leaflet. In Fig. 2 the mixed state is unstable (i.e. concave down) to both R and AR demixing modes. Although the equilibrium phases are R, metastable AR phases will be accessed first if the AR mode is fastest.

Fig. 3 shows R/AR slices through  $f^{[ann.]}(\bar{\phi}^t, \bar{\phi}^b)$  for some different state points (marked in Fig. 4b). For the lowest direct coupling  $B$ , the *equilibrium* phase is AR demixed. Upon increasing  $B$  (penalising AR), R demixing becomes equilibrium (but with the mixed state *metastable* against it), and then AR demixing is lost. For the largest  $B$  the mixed state is *unstable* to R demixing. Fig. 3 also shows that the leaflet compositions of the AR phases do

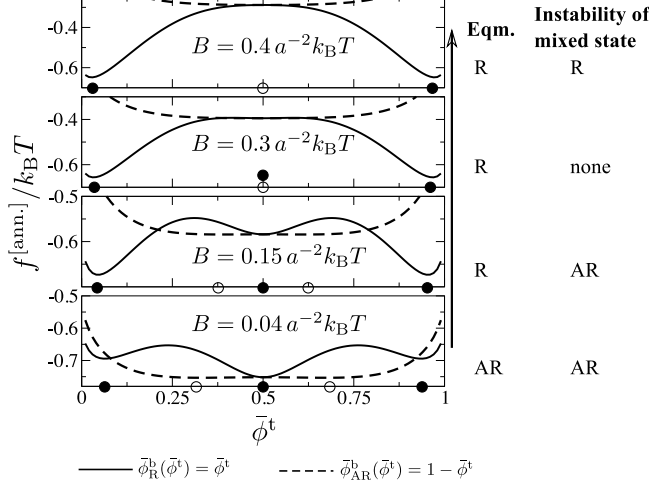


FIG. 3. R and AR slices through  $f^{[\text{ann.}]}(\bar{\phi}^t, \bar{\phi}^b)$  for the sequence of state points of increasing direct coupling in Fig. 4b. Filled (empty) circles mark minima in the R (AR) mode.

not coincide with the R phases, as they are affected differently by the inter-leaflet couplings. Increasing  $B$  brings the AR demixed minima progressively inward towards  $\bar{\phi}^t = 0.5$  until they disappear, but moves the R demixed minima outward, towards  $\bar{\phi}^t = 0, 1$ .

### C. Instability criteria

Instability to demixing requires negative curvature of  $f^{[\text{ann.}]}$ . For the R/AR modes, we define  $f^{\text{m}[\text{ann.}]}(\bar{\phi}^t) \equiv f^{[\text{ann.}]}(\bar{\phi}^t, \bar{\phi}_m^b(\bar{\phi}^t))$  where  $m = \text{R, AR}$  labels the demixing mode. Hence, instability of a given mode  $m$  at the equimolar ‘mixed state’ requires  $\left. \frac{d^2}{d\bar{\phi}^{t2}} f^{\text{m}[\text{ann.}]} \right|_{\bar{\phi}^t=0.5} < 0$ . We find

$$\left. \frac{d^2}{d\bar{\phi}^{t2}} f^{\text{R}[\text{ann.}]} \right|_{0.5} = \frac{4}{\beta} (1 + e^{-\beta\sigma}) - 16 \left( V + \frac{(\Delta_0)^2 J \kappa}{4(2J + \kappa)} \right), \quad (6a)$$

$$\left. \frac{d^2}{d\bar{\phi}^{t2}} f^{\text{AR}[\text{ann.}]} \right|_{0.5} = \frac{4}{\beta} (1 + e^{\beta\sigma}) - 16V, \quad (6b)$$

with  $\beta^{-1} \equiv k_B T$ , where

$$\sigma \equiv \frac{1}{2} (H_{SU} + H_{US} - H_{SS} - H_{UU}) \quad (7a)$$

$$= -\frac{(\Delta_0)^2 \kappa^2 (J - B)}{2(2J + \kappa)(2B + \kappa)}, \quad (7b)$$

is the (mean-field) energy per site for converting two sites from R to AR ( $SS + UU \rightarrow SU + US$ ). The curvatures contain a positive entropy-like part inhibiting instability and a negative enthalpic part promoting it. The more negative is  $\left. \frac{d^2}{d\bar{\phi}^{t2}} f^{\text{m}[\text{ann.}]} \right|_{0.5}$ , the stronger is the thermodynamic driving force for instability to demixing mode  $m$ .

$\sigma$  controls the excess proportion  $x_{\text{reg}}^{\text{mixed}}$  of pairwise R amphiphile pairs present in the mixed state (25). Evaluating the  $N_\alpha$  at  $\bar{\phi}^b = \bar{\phi}^t = 0.5$  gives

$$x_{\text{reg}}^{\text{mixed}} \equiv \frac{N_{SS} + N_{UU} - N_{SU} - N_{US}}{N} = \tanh \frac{\beta\sigma}{2}. \quad (8)$$

Hence  $J > B$  ( $\sigma < 0$ ) gives  $x_{\text{reg}}^{\text{mixed}} < 0$ , implying mostly pairwise AR in the mixed state (as measured in (12)), i.e. most amphiphiles aligned with the opposite species. The Boltzmann factors  $e^{\pm\beta\sigma}$  in Eqs. 6a and 6b control the loss of configurational entropy, relative to the mixed state, for creating excess pairwise R (AR) sites required by the R (AR) demixing mode. For example, increasing  $J$  (decreasing  $\sigma$ ) promotes greater pairwise AR in the mixed state, thus decreasing the entropic penalty in Eq. 6b for accessing the AR demixing mode.

The enthalpic part for the R mode (Eq. 6a) is augmented by the hydrophobic mismatch penalty  $J$ , for mixing  $SS$  and  $UU$  sites. But since  $J$  also appears in  $\sigma$ , it can increase the entropy-like part enough to render the mixed state metastable against R demixing (as for the middle two panels of Fig. 3) (26).  $J$  promotes demixing of pairwise R sites *once they are created*, but also increases the cost of creating R sites in the first place, thus causing a free energy barrier for R demixing. In contrast, the Ising-like interaction  $V$  trivially increases the instability.

#### D. Growth rates

When, as in Fig. 2, the mixed state is unstable to *both* R and AR modes, initial demixing will be determined by a competition of the modes. This can be studied by comparing their growth rates in a linear stability analysis of a Ginzburg-Landau (G-L) free energy (27)  $F_{\text{G-L}} = \int d^2r ((f/a^2) + f_{\text{grad}})$ , with the gradient terms

$$f_{\text{grad}} = \frac{1}{2} \tilde{J}(\nabla \bar{d})^2 + V(\nabla \bar{\phi}^{\text{t}})^2 + V(\nabla \bar{\phi}^{\text{b}})^2, \quad (9)$$

arising from the nearest-neighbour interactions that depend on the total thickness and leaflet compositions. The detailed calculations are given in Appendix B. We obtain wavenumber dependent growth rates  $\omega^{\text{m}}(q)$  whose maxima over  $q$  yield  $\omega_{\text{max}}^{\text{m}}$ . The difference  $\Delta\omega \equiv \omega_{\text{max}}^{\text{R}} - \omega_{\text{max}}^{\text{AR}}$  determines which mode is faster and thus dominates the initial demixing.

#### E. Stability diagrams

Combining the preceding analyses, Fig. 4 shows the dependence of equilibrium phases, R/AR instabilities, and their relative growth rates on direct and indirect couplings, for varying choices of the Ising-like interaction  $V$  and difference in ideal lengths  $\Delta_0$ .

*Weak mismatch* ( $\Delta_0 = 1a$ ): For  $V = 0.3 k_{\text{B}}T$  and weak thickness mismatch, no demixing takes place since  $V < V_0$  (Fig. 4a), while  $V = 0.6 k_{\text{B}}T$  (Fig. 4c) induces demixing as in the MF Ising model. The equilibrium state is R demixed, but both modes are unstable and for strong enough hydrophobic mismatch, the AR mode can be *faster* (red). Hence, the state point marked in Fig. 4c will initially undergo spinodal decomposition in the AR mode, accessing the metastable AR minima (Fig. 2). The bilayer subsequently requires *nucleation* to reach the equilibrium R minima, despite having begun in the ‘spinodal’ region.

*Strong mismatch* ( $\Delta_0 = 2a$ ): Increasing  $\Delta_0$  strengthens both the indirect and direct couplings (physically, this could arise from increasing both the degree of length mismatch and difference in unsaturation of the species’ tails). In contrast to the weak mismatch case, for  $V = 0.3 k_{\text{B}}T$  (Fig. 4b) the inter-leaflet couplings can induce demixing although (since  $V < V_0$ ) *neither* leaflet would demix ‘on its own’ (3, 7) (i.e. without coupling). A large hydrophobic penalty  $J$  promotes pairwise AR which, due to the doubled effective Ising interaction between  $SU$  and  $US$  pairs ( $2V > V_0$ ), leads to AR demixing. There is even a

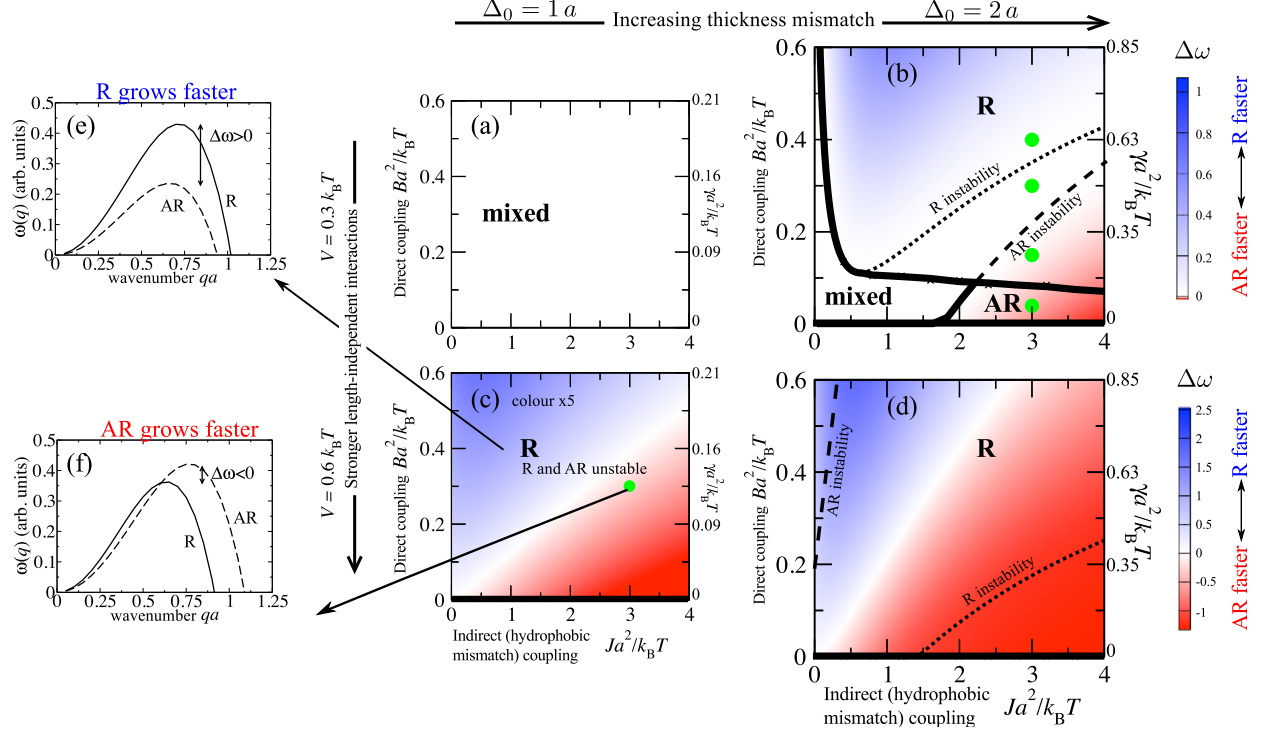


FIG. 4. (a)–(d) Stability diagrams in indirect and direct couplings  $J, B$ , at varying values of the Ising interaction strength  $V$  and the difference in ideal thicknesses. Thick lines and bold labels indicate the equilibrium phase R, AR or mixed. Thinner lines denote instability of an equimolar mixture to R/AR modes, the labels appearing on the side of the lines to which they refer. **Secondary axis:** approximate values of the inter-leaflet mismatch free energy per area  $\gamma$ . **Colours:** from linear stability analysis of the equimolar mixture,  $\Delta\omega > 0$  (R mode faster, blue),  $\Delta\omega < 0$  (AR faster, red). In (c) the colour scale range is reduced by a factor 5 from that indicated on (d). **Green dots:** in (b) correspond to Fig. 3, in (c) corresponds to Fig. 2. (e) and (f) show illustrative  $q$ -dependent growth rates.

small region in which AR demixing is the *equilibrium* state. Increasing the direct coupling  $B$  favours R demixing, enhanced by hydrophobic thickness mismatch between  $SS$  and  $UU$  sites – but large  $J$  renders the mixed state metastable, not unstable, against equilibrium R demixing (within the **R** region but outside the ‘R instability’ line). For  $V = 0.6 k_B T$  (Fig. 4d), demixing always takes place since  $V > V_0$ .

#### IV. DISCUSSION

We have modelled the coupled leaflets of a bilayer in which hydrophobic mismatch causes an indirect coupling  $J$ , promoting antiregistration (AR). This competes with a direct coupling  $B$ , arising from tail structure mismatch, which promotes trans-midplane registration (R) of like species. These competing interactions lead to rich free energy landscapes that imply complex kinetics for R/AR demixing. As simulated in (13, 14), increased hydrophobic mismatch favours AR demixing, typically a metastable, not equilibrium, state.

The predictions depend on the interplay of  $J$  with  $B$ , the latter approximately mapping to

the inter-leaflet mismatch free energy per area  $\gamma$ . For typical phospholipids ( $J \sim 2 a^{-2} k_B T$ ) with a significant lipid length mismatch  $\Delta_0 \sim 0.8 \text{ nm}$  ( $\sim 1 a$ ), Fig. 4c may apply. Taking  $\gamma \approx 0.15 k_B T \text{ nm}^{-2} \approx 0.1 a^{-2} k_B T$  (3, 22) (so  $B \approx 0.23 a^{-2} k_B T$ ) on that figure implies comparable R/AR growth rates. However, (4) argues for  $\gamma \sim 0.01 a^{-2} k_B T$  ( $B \approx 0.02 a^{-2} k_B T$ ). Then, the mixed bilayer is likely to first access a metastable AR demixed state, paradoxically requiring nucleation to reach R equilibrium, despite having begun in the spinodal region (28). Both estimates of  $\gamma$  suggest  $B < J$ , implying the mixed state is mostly *pairwise* AR (Eq. 8), in agreement with (12).

Hydrophobic mismatch has both intra- and inter-leaflet effects, encouraging demixing but also indirectly coupling the leaflets. This dual role is absent in previous phenomenological theories (3, 7), which *a priori* consider only purely intra- and purely inter-leaflet couplings.

Macroscopic domains should typically be registered at equilibrium, since the hydrophobic mismatch energy scales as domain edge while the direct coupling scales as area (3). Registration observations in LO-LD (10) may indicate that nucleation barriers to R demixing are typically surmountable. In contrast, AFM experiments (15) have shown small R gel domains converting to an AR state. In light of our results, this could indicate decay of subcritical R nuclei into a metastable AR state. It is likely that metastable AR free energy minima are generically implicated in observations of full or partial antiregistration (13–15), and in the apparent dependence of domain registration on thermal history (15). Standard fluorescence microscopy or AFM might not distinguish side-by-side complementary AR domains (*SU* alongside *US*), which would be of identical total thickness and similar fluorescence, thus appearing homogeneous and potentially disguising any initial AR demixing step. The rich free energy landscapes of coupled leaflets imply equally rich *kinetics* for registration and antiregistration, whose study is particularly important given the nonequilibrium nature of the cell membrane. The free energy can also be used to find phase equilibria under given constraints on overall leaflet compositions, permission of flip-flop, etc.

We have focused on approximate phospholipid parameters, but the phenomenology also applies to polymeric bilayers (29, 30), whose properties and hence predicted phase behaviour may be quite different. ‘Hybrid’ lipids, where one tail varies in saturation/length relative to the other, can act as linactants (31). Further work is required to establish their effects on the physics studied here, but we speculate that such linactants could favour registration, by diminishing the energy cost for the thickness mismatch at registered domain boundaries. We have implicitly considered a flat membrane, but membrane curvature can drive domain formation (32) and has also been proposed as a factor in domain inter-leaflet coupling (21). In principle our theory could be supplemented with curvature terms (5), although it is not obvious whether these could be derived from microscopic considerations as is our bulk free energy, or would be phenomenological. Finally, although our calculations are limited to the mean-field and our dynamical analysis to the linear regime, preliminary comparisons with direct Monte Carlo simulation of the model suggest good agreement. A detailed simulation and theory study of the kinetics involved will be given in an upcoming publication.

## Appendix A: Derivation of mean-field free energy

The underlying lattice model is a  $L^2 = N$  square lattice of sites with top (t) and bottom (b) leaflet amphiphiles, whose Hamiltonian is given by Eq. 1. The exact partition function

is

$$Z = \sum_{\{\hat{\phi}_i^t, \hat{\phi}_i^b\}}^{\text{constrained}} \int \mathcal{D}\Delta \mathcal{D}d \exp(-\beta H), \quad (\text{A1})$$

where the sum is constrained by the average leaflet compositions  $\bar{\phi}^{t(b)} \equiv N_S^{t(b)}/N$ , and we have defined  $\mathcal{D}\Delta \equiv \prod_i d\Delta_i$  and  $\mathcal{D}d \equiv \prod_i dd_i$ . The free energy is related to the partition function by

$$fN = -k_B T \ln Z, \quad (\text{A2})$$

and our aim is to find a mean-field approximation to the free energy per site  $f$  that depends only on coarse-grained variables for the composition and thickness of each leaflet of the bilayer.

### 1. Mean-field (on-site) approximation

We use a mean-field approximation, ignoring correlations between neighbouring sites. This requires approximating the neighbour interaction terms of  $H$  (those involving  $V$  and  $\tilde{J}$ ) with on-site terms. For the  $\tilde{J}$  term, we define the mean-field bilayer thickness  $\bar{d} \equiv \sum d_i/N$  and write

$$\begin{aligned} \sum_{\langle i,j \rangle} (d_i - d_j)^2 &= \sum_{\langle i,j \rangle} ([d_i - \bar{d}] - [d_j - \bar{d}])^2 \\ &= \sum_{\langle i,j \rangle} ([d_i - \bar{d}]^2 + [d_j - \bar{d}]^2 - 2[d_i - \bar{d}][d_j - \bar{d}]) \\ &\approx \sum_i 4(d_i - \bar{d})^2. \end{aligned} \quad (\text{A3})$$

The mean-field approximation consists in assuming the cross term  $[d_i - \bar{d}][d_j - \bar{d}]$  to sum to zero, i.e. that  $d_i$  and  $d_j$  are uncorrelated.

For the Ising-like term in (say) the top leaflet, the interaction matrix  $V_{\alpha\beta}$  permits a mapping to the Ising model. Define the exchange parameter  $J^{\text{Ising}}$  (unrelated to the  $J$  in our model) and the ‘spin’ variable  $s_i^t \equiv 2\hat{\phi}_i^t - 1$ , which takes the value 1 or  $-1$ , and consider the Ising model in which the interaction energy between spins  $i$  and  $j$  is  $E_{ij} = -J^{\text{Ising}} s_i^t s_j^t$ . In the mean-field approximation, the total energy of this Ising model is  $E \approx -2J^{\text{Ising}}(\bar{s}^t)^2 N$  where  $\bar{s}^t$  is the mean value of the spin. This can be written as

$$E = \sum_{\langle i,j \rangle} -J^{\text{Ising}} s_i^t s_j^t \approx \sum_i -2J^{\text{Ising}} s_i^t \bar{s}^t. \quad (\text{A4})$$

The excess interaction energy for unlike versus like neighbours in the Ising model is  $E_{ij}|_{s_i^t = -s_j^t} - E_{ij}|_{s_i^t = s_j^t} = 2J^{\text{Ising}}$ . For  $V_{\alpha\beta}$ , this difference is given by  $V \equiv V_{10} - \frac{1}{2}(V_{00} + V_{11})$ . Hence equivalence with the Ising model is established by setting  $V = 2J^{\text{Ising}}$ . Therefore, in the mean-field approximation of our lattice Hamiltonian, we can write

$$\sum_{\langle i,j \rangle} V_{\hat{\phi}_i^t \hat{\phi}_j^t} \approx \sum_i -V s_i^t \bar{s}^t = \sum_i -V s_i^t (2\bar{\phi}^t - 1), \quad (\text{A5})$$

and similarly for the bottom leaflet. The mean-field (i.e. on-site) approximation to the Hamiltonian is thus given by

$$H \approx H_{\text{MF}} = \sum_i H_i , \quad (\text{A6})$$

where

$$H_i = -V s_i^t (2\bar{\phi}^t - 1) - V s_i^b (2\bar{\phi}^b - 1) + \frac{1}{2} J (d_i - \bar{d})^2 + \frac{1}{2} B (\Delta_i)^2 + \frac{1}{2} \kappa ((\ell_i^t - \ell_0^t)^2 + (\ell_i^b - \ell_0^b)^2) , \quad (\text{A7})$$

and  $J \equiv 4\tilde{J}$ .

## 2. Site types

We now note that, given a mixture of  $S$  and  $U$  species in each leaflet, there are four possible site types,  $\alpha \in \{SS, UU, SU, US\}$  where an  $AB$  site contains species  $A$  on the top and  $B$  on the bottom.  $SS$  and  $UU$  sites are pairwise registered, while  $SU$  and  $US$  sites are pairwise antiregistered. All sites of type  $\alpha$  share the same values of the species-dependent constants  $s_i^t$ ,  $s_i^b$ ,  $\ell_0^t$  and  $\ell_0^b$  in their  $H_i$ . We can therefore express the total mean-field Hamiltonian  $H_{\text{MF}}$  as a sum over the noninteracting site-level Hamiltonians

$$H_{\text{MF}} = \sum_{\alpha} \sum_{j_{\alpha}}^{N_{\alpha}} H_{j_{\alpha}} , \quad (\text{A8})$$

where  $j_{\alpha}$  labels the  $j$ th out of  $N_{\alpha}$  sites of type  $\alpha$ , and

$$H_{j_{\alpha}} = \pm V (2\bar{\phi}^t - 1) \pm V (2\bar{\phi}^b - 1) + \frac{1}{2} J (d_{j_{\alpha}} - \bar{d})^2 + \frac{1}{2} B (\Delta_{j_{\alpha}})^2 + \frac{1}{2} \kappa ((\ell_{j_{\alpha}}^t - \ell_0^t)^2 + (\ell_{j_{\alpha}}^b - \ell_0^b)^2) . \quad (\text{A9})$$

Here,  $\ell_0^t = \ell_{A0}$  and  $\ell_0^b = \ell_{B0}$  for  $\alpha = AB$ , and the  $\pm$  are  $--$  for  $\alpha = SS$ ,  $++$  ( $UU$ ),  $-+$  ( $SU$ ) and  $+-$  ( $US$ ).

The sum over the top and bottom leaflet configurations can be rewritten as a sum over the occupancies of the set of site types, i.e.

$$\sum_{\{\phi_i^t, \phi_i^b\}}^{\text{constr.}} = \sum_{\{N_{\alpha}\}}^{\text{constr.}} \frac{1}{\prod_{\alpha} N_{\alpha}!} , \quad (\text{A10})$$

where the factorials avoid overcounting indistinguishable configurations and the sum is constrained by Eqs. 2c–2e.

Defining  $\mathcal{D}\Delta_{\alpha} \equiv \prod_{j_{\alpha}} d\Delta_{j_{\alpha}}$  and  $\mathcal{D}d_{\alpha} \equiv \prod_{j_{\alpha}} dd_{j_{\alpha}}$ , the mean-field partition function  $Z_{\text{MF}}$  is

$$Z_{\text{MF}} = \sum_{\{N_{\alpha}\}}^{\text{constr.}} \frac{1}{\prod_{\alpha} N_{\alpha}!} \prod_{\alpha} \int \mathcal{D}\Delta_{\alpha} \mathcal{D}d_{\alpha} \exp(-\beta \sum_{j_{\alpha}}^{N_{\alpha}} H_{j_{\alpha}}) . \quad (\text{A11})$$

Since all sites are now independent of one another, the integral may be rewritten in terms of the partition function for a single site of type  $\alpha$ . Additionally, the constraints Eqs. 2c–2e allow the Ising interaction  $V$  to be factored out. We thus have

$$Z_{\text{MF}} = \sum_{\{N_\alpha\}}^{\text{constr.}} \exp(-\beta N V^*(\bar{\phi}^t, \bar{\phi}^b)) \frac{\prod_\alpha Z_\alpha^{N_\alpha}}{\prod_\alpha N_\alpha!}, \quad (\text{A12})$$

where we have defined

$$V^*(\bar{\phi}^t, \bar{\phi}^b) \equiv -2V(\bar{\phi}^t - \bar{\phi}^b)^2 - 2V(\bar{\phi}^t + \bar{\phi}^b - 1)^2. \quad (\text{A13})$$

The single-site thickness partition function is given by

$$Z_\alpha = \int d\Delta_\alpha dd_\alpha \exp(-\beta H_\alpha), \quad (\text{A14})$$

in which

$$H_\alpha = \frac{1}{2}J(d_\alpha - \bar{d})^2 + \frac{1}{2}B(\Delta_\alpha)^2 + \frac{1}{2}\kappa((\ell_\alpha^t - \ell_0^{t\alpha})^2 + (\ell_\alpha^b - \ell_0^{b\alpha})^2), \quad (\text{A15})$$

now contains only the thickness-dependent interactions.

### 3. Self-consistency, free energy

For self-consistency of the average bilayer thickness  $\bar{d}$  and the average difference  $\bar{\Delta}$ , we require the integrations over  $d_\alpha$ ,  $\Delta_\alpha$  to be performed subject to Eqs. 2a, 2b. Since these integrals are Gaussian, and the constraints Eqs. 2a, 2b are linear, the integrations can be performed exactly to yield

$$\prod_\alpha Z_\alpha^{N_\alpha} = \exp(-\beta \sum_\alpha N_\alpha H_\alpha\{d_\alpha^*, \Delta_\alpha^*\}), \quad (\text{A16})$$

where  $\{d_\alpha^*, \Delta_\alpha^*\}$  minimise  $\sum_\alpha N_\alpha H_\alpha$  subject to Lagrange multipliers enforcing Eqs. 2a, 2b.

Now the mean-field partition function can be written

$$Z_{\text{MF}} = \sum_{\{N_\alpha\}}^{\text{constr.}} \exp\left(-\beta \left[ N V^*(\bar{\phi}^t, \bar{\phi}^b) + \sum_\alpha N_\alpha (H_\alpha\{d_\alpha^*, \Delta_\alpha^*\} + k_B T \ln N_\alpha) \right]\right) \equiv \sum_{\{N_\alpha\}}^{\text{constr.}} \exp(-\beta N \tilde{f}), \quad (\text{A17})$$

where Stirling's approximation has been used ( $\ln N_\alpha! \approx N_\alpha \ln N_\alpha - N_\alpha$ ), contributing an irrelevant constant.

The three constraints Eqs. 2c–2e leave only one  $N_\alpha$  over which to sum. For this we perform a saddle-point approximation, which is equivalent to removing the sum and setting  $\{N_\alpha\}$  to their values that minimise  $\tilde{f}$  subject to Eqs. 2c–2e. This yields

$$Z_{\text{MF}} \approx \exp(-\beta N \tilde{f}^*), \quad (\text{A18})$$

where  $\tilde{f}^*$  is the minimised value of  $\tilde{f}$ . Then, by Eq. A2, our desired free energy per site  $f(\bar{\phi}^t, \bar{\phi}^b, \bar{d}, \bar{\Delta})$  is given by  $\tilde{f}^*$ .

The steps described above can be summarised compactly by stating that the free energy  $f(\bar{\phi}^t, \bar{\phi}^b, \bar{d}, \bar{\Delta})$  per site is given by minimising

$$f'N = \sum_{\alpha} N_{\alpha} (H_{\alpha} + k_{\text{B}}T \ln N_{\alpha}) - 2VN(\bar{\phi}^{\text{t}} - \bar{\phi}^{\text{b}})^2 - 2VN(\bar{\phi}^{\text{t}} + \bar{\phi}^{\text{b}} - 1)^2 \quad (\text{A19})$$

over  $\{d_{\alpha}, \Delta_{\alpha}, N_{\alpha}\}$  subject to Lagrange multipliers enforcing Eqs. 2a–2e, as written in Eq. 3. The variables fixed in the minimisation procedure are

$$d_{SS} = \bar{d} + \frac{\kappa\Delta_0}{2J + \kappa}(2 - \bar{\phi}^{\text{t}} - \bar{\phi}^{\text{b}}), \quad (\text{A20a})$$

$$d_{UU} = \bar{d} - \frac{\kappa\Delta_0}{2J + \kappa}(\bar{\phi}^{\text{t}} + \bar{\phi}^{\text{b}}), \quad (\text{A20b})$$

$$d_{SU} = d_{US} = \bar{d} - \frac{\kappa\Delta_0}{2J + \kappa}(\bar{\phi}^{\text{t}} + \bar{\phi}^{\text{b}} - 1), \quad (\text{A20c})$$

$$\Delta_{SS} = \Delta_{UU} = \bar{\Delta} - \frac{\kappa\Delta_0}{2B + \kappa}(\bar{\phi}^{\text{t}} - \bar{\phi}^{\text{b}}), \quad (\text{A20d})$$

$$\Delta_{SU} = \bar{\Delta} - \frac{\kappa\Delta_0}{2B + \kappa}(\bar{\phi}^{\text{t}} - \bar{\phi}^{\text{b}} - 1), \quad (\text{A20e})$$

$$\Delta_{US} = \bar{\Delta} - \frac{\kappa\Delta_0}{2B + \kappa}(\bar{\phi}^{\text{t}} - \bar{\phi}^{\text{b}} + 1), \quad (\text{A20f})$$

$$N_{SS}/N = A, \quad (\text{A20g})$$

$$N_{UU}/N = A + 1 - \bar{\phi}^{\text{t}} - \bar{\phi}^{\text{b}}, \quad (\text{A20h})$$

$$N_{SU}/N = -A + \bar{\phi}^{\text{t}}, \quad (\text{A20i})$$

$$N_{US}/N = -A + \bar{\phi}^{\text{b}}. \quad (\text{A20j})$$

We have defined

$$A \equiv \frac{2\bar{\phi}^{\text{t}}\bar{\phi}^{\text{b}}}{\bar{\phi}^* \left(1 + \sqrt{1 + \frac{4\bar{\phi}^{\text{t}}\bar{\phi}^{\text{b}}(\exp[-2\beta\sigma]-1)}{(\bar{\phi}^*)^2}}\right)}, \quad (\text{A21})$$

where

$$\bar{\phi}^* \equiv \bar{\phi}^{\text{t}} + \bar{\phi}^{\text{b}} + e^{-2\beta\sigma}(1 - \bar{\phi}^{\text{t}} - \bar{\phi}^{\text{b}}), \quad (\text{A22})$$

and

$$\begin{aligned} \sigma &\equiv \frac{1}{2}(H_{SU} + H_{US} - H_{SS} - H_{UU}) \\ &= -\frac{\Delta_0^2\kappa^2(J - B)}{2(2J + \kappa)(2B + \kappa)}, \end{aligned} \quad (\text{A23})$$

is the energy change per site for converting two R sites into two AR sites. The expected self-consistency requirements are fulfilled; for example,  $\bar{\phi}^{\text{b}} = \bar{\phi}^{\text{t}} \rightarrow 1$  (forcing all sites to be of *SS* type) leads to  $d_{SS} \rightarrow \bar{d}$ .

To construct the coarse-grained free energy  $f(\bar{\phi}^{\text{t}}, \bar{\phi}^{\text{b}}, \bar{d}, \bar{\Delta})$ , we insert Eqs. A20–A23 into Eq. A19. We find

$$\begin{aligned}
& f(\bar{\phi}^t, \bar{\phi}^b, \bar{d}, \bar{\Delta}) = \\
& k_{\text{B}}T \left[ A \ln A + (A + 1 - \bar{\phi}^t - \bar{\phi}^b) \ln (A + 1 - \bar{\phi}^t - \bar{\phi}^b) + (\bar{\phi}^t - A) \ln (\bar{\phi}^t - A) + (\bar{\phi}^b - A) \ln (\bar{\phi}^b - A) \right] \\
& + \frac{1}{2} \kappa \left[ (\bar{d} - d_0)^2 + \Delta_0 \left( (\bar{\phi}^t + \bar{\phi}^b - 1)(d_0 - \bar{d}) - (\bar{\phi}^t - \bar{\phi}^b) \bar{\Delta} + \frac{1}{2} \Delta_0 \right) \right] + \frac{1}{4} \bar{\Delta}^2 (2B + \kappa) \\
& + \frac{\kappa^2 \Delta_0^2}{2(2B + \kappa)(2J + \kappa)} \left[ (2A - 2\bar{\phi}^t \bar{\phi}^b) (J - B) - (\bar{\phi}^t + \bar{\phi}^b - \bar{\phi}^{t2} - \bar{\phi}^{b2}) (J + B + \kappa) \right] \\
& - 2V(\bar{\phi}^t - \bar{\phi}^b)^2 - 2V(\bar{\phi}^t + \bar{\phi}^b - 1)^2, \tag{A24}
\end{aligned}$$

where  $\Delta_0 \equiv \ell_{S0} - \ell_{U0}$ ,  $d_0 \equiv \ell_{S0} + \ell_{U0}$ .

Upon further minimising  $f$  over the MF thickness variables  $\bar{d}$  and  $\bar{\Delta}$ , we obtain  $f^{[\text{ann.}]}(\bar{\phi}^t, \bar{\phi}^b)$ , which determines local and global minima of the free energy (see e.g. Figs. 2, 3). The annealed thickness variables are

$$\bar{d}^{[\text{ann.}]} = \Delta_0(\bar{\phi}^t + \bar{\phi}^b - 1) + d_0, \tag{A25a}$$

$$\bar{\Delta}^{[\text{ann.}]} = \frac{\kappa \Delta_0 (\bar{\phi}^t - \bar{\phi}^b)}{2B + \kappa}, \tag{A25b}$$

giving

$$\begin{aligned}
& f^{[\text{ann.}]}(\bar{\phi}^t, \bar{\phi}^b) = \\
& k_{\text{B}}T \left[ A \ln A + (A + 1 - \bar{\phi}^t - \bar{\phi}^b) \ln (A + 1 - \bar{\phi}^t - \bar{\phi}^b) + (\bar{\phi}^t - A) \ln (\bar{\phi}^t - A) + (\bar{\phi}^b - A) \ln (\bar{\phi}^b - A) \right] \\
& + \frac{1}{2} \frac{B \kappa \Delta_0^2 (\bar{\phi}^t + \bar{\phi}^b)}{2B + \kappa} (2 - \bar{\phi}^t - \bar{\phi}^b) - \sigma (2A + [\bar{\phi}^t + \bar{\phi}^b][1 - \bar{\phi}^t - \bar{\phi}^b]) \\
& - 2V(\bar{\phi}^t - \bar{\phi}^b)^2 - 2V(\bar{\phi}^t + \bar{\phi}^b - 1)^2. \tag{A26}
\end{aligned}$$

## Appendix B: Ginzburg-Landau analysis

$f(\bar{\phi}^t, \bar{\phi}^b, \bar{d}, \bar{\Delta})$  is the coarse-grained free energy per site. This can serve as the ‘Landau part’ of a Ginzburg-Landau type free energy  $F_{\text{G-L}}$  to study kinetics

$$F_{\text{G-L}} = \int d^2r \left( \frac{f}{a^2} + f_{\text{grad}} \right), \tag{B1}$$

where

$$f_{\text{grad}} = \frac{\tilde{J}}{2} (\nabla \bar{d})^2 + V (\nabla \bar{\phi}^t)^2 + V (\nabla \bar{\phi}^b)^2. \tag{B2}$$

This gradient contribution depends on the terms of the Hamiltonian by which laterally neighbouring sites interact. The composition gradient term in each leaflet involving  $V$  is simply that for the MF Ising model (33), and the thickness gradient term involving  $\tilde{J}$  is the corresponding term of Eq. 1 in the limit of small lattice spacing.

We will study the instabilities at a reference ‘mixed state’ defined by  $\bar{\phi}^b = \bar{\phi}^t = 0.5$ ,  $\bar{\Delta} = 0$ ,  $\bar{d} = d_0$ , applying small perturbations to this mixed state and determining the resultant

change in  $F_{\text{G-L}}$ . The thermodynamic driving force for instability to demixing, determined by  $f$ , competes with the gradient terms  $f_{\text{grad}}$  which penalise the resultant inhomogeneity. Combining these with evolution equations for composition and thickness, we find preferred lengthscales for initial demixing, and associated rates, that can be compared between the R and AR modes.

A perturbation is described by  $\delta\bar{\phi}^t$ ,  $\delta\bar{\phi}^b$ ,  $\delta\bar{\ell}^t$ ,  $\delta\bar{\ell}^b$ . Considering separately the R mode (in which  $\bar{\phi}_{\text{R}}^b(\bar{\phi}^t) = \bar{\phi}^t$ ,  $\bar{\Delta} = 0$  and  $\delta\bar{\ell}^b = \delta\bar{\ell}^t$ ) and the AR mode (in which  $\bar{\phi}_{\text{AR}}^b(\bar{\phi}^t) = 1 - \bar{\phi}^t$ ,  $\bar{d} = d_0$  and  $\delta\bar{\ell}^b = -\delta\bar{\ell}^t$ ), we now apply linear stability analysis to perturbations governed by Eq. B1, to determine which mode initially grows fastest.

### 1. Evolution of perturbations

The free energy change due to a perturbation in mode  $m$  is

$$\delta F_{\text{G-L}}^m = \frac{1}{2} \int d^2r \left( \begin{pmatrix} \delta\bar{\phi}^t \\ \delta\bar{\ell}^t \end{pmatrix} \cdot \underline{\underline{C}}^m \cdot \begin{pmatrix} \delta\bar{\phi}^t \\ \delta\bar{\ell}^t \end{pmatrix} + \nabla \begin{pmatrix} \delta\bar{\phi}^t \\ \delta\bar{\ell}^t \end{pmatrix} \cdot \underline{\underline{P}}^m \cdot \nabla \begin{pmatrix} \delta\bar{\phi}^t \\ \delta\bar{\ell}^t \end{pmatrix} \right), \quad (\text{B3})$$

where  $m = \text{R}, \text{AR}$  and the matrices  $\underline{\underline{C}}^m$  and  $\underline{\underline{P}}^m$  respectively contain the bulk and gradient free energy terms:

$$a^2 \underline{\underline{C}}^{\text{R}} = \begin{bmatrix} f_{\bar{\phi}^t \bar{\phi}^t}^{\text{R}} & 2f_{\bar{d} \bar{\phi}^t}^{\text{R}} \\ 2f_{\bar{d} \bar{\phi}^t}^{\text{R}} & 4f_{\bar{d} \bar{d}}^{\text{R}} \end{bmatrix} = \begin{bmatrix} \left( 4k_{\text{B}}T [e^{-\beta\sigma} + \beta\sigma + 1] + \frac{2\kappa^2 \Delta_0^2 (B+\kappa+J)}{(2B+\kappa)(2J+\kappa)} - 16V \right) & -2\kappa\Delta_0 \\ -2\kappa\Delta_0 & 2\kappa \end{bmatrix}, \quad (\text{B4a})$$

$$a^2 \underline{\underline{C}}^{\text{AR}} = \begin{bmatrix} f_{\bar{\phi}^t \bar{\phi}^t}^{\text{AR}} & 2f_{\bar{\Delta} \bar{\phi}^t}^{\text{AR}} \\ 2f_{\bar{\Delta} \bar{\phi}^t}^{\text{AR}} & 4f_{\bar{\Delta} \bar{\Delta}}^{\text{AR}} \end{bmatrix} = \begin{bmatrix} \left( 4k_{\text{B}}T [e^{\beta\sigma} - \beta\sigma + 1] + \frac{2\kappa^2 \Delta_0^2 (B+\kappa+J)}{(2B+\kappa)(2J+\kappa)} - 16V \right) & -2\kappa\Delta_0 \\ -2\kappa\Delta_0 & 2(2B + \kappa) \end{bmatrix}, \quad (\text{B4b})$$

$$\underline{\underline{P}}^{\text{R}} = \begin{bmatrix} 4V & 0 \\ 0 & 4\tilde{J} \end{bmatrix}, \quad \underline{\underline{P}}^{\text{AR}} = \begin{bmatrix} 4V & 0 \\ 0 & 0 \end{bmatrix}. \quad (\text{B4c})$$

$f^{\text{R}}(\bar{\phi}^t, \bar{d})$  represents  $f$  evaluated for  $\bar{\phi}_{\text{R}}^b(\bar{\phi}^t) = \bar{\phi}^t$ ,  $\bar{\Delta} = 0$ , and  $f^{\text{AR}}(\bar{\phi}^t, \bar{\Delta})$  represents  $f$  evaluated for  $\bar{\phi}_{\text{AR}}^b(\bar{\phi}^t) = 1 - \bar{\phi}^t$ ,  $\bar{d} = d_0$ . Subscripts indicate derivatives evaluated at the mixed state, i.e.  $\bar{\phi}^t = 0.5$ ,  $\bar{d} = d_0$ ,  $\bar{\Delta} = 0$ .

Since composition is conserved, it evolves (34) via

$$\frac{\partial \delta\bar{\phi}^t}{\partial t} = M \nabla^2 (C_{11}^m \delta\bar{\phi}^t + C_{12}^m \delta\bar{\ell}^t - P_{11}^m \nabla^2 \delta\bar{\phi}^t - P_{12}^m \nabla^2 \delta\bar{\ell}^t), \quad (\text{B5})$$

where the mobility  $M$  sets the timescale.

We assume thickness to behave in a nonconserved fashion so that it evolves relaxationally (34), via

$$\frac{\partial \delta\bar{\ell}^t}{\partial t} = -\eta (C_{21}^m \delta\bar{\phi}^t + C_{22}^m \delta\bar{\ell}^t - P_{21}^m \nabla^2 \delta\bar{\phi}^t - P_{22}^m \nabla^2 \delta\bar{\ell}^t), \quad (\text{B6})$$

where the mobility  $\eta$  incorporates frictional forces involved in length stretching and compression of amphiphiles (in principle it can acquire wavenumber dependence via coupling to the conserved solvent flow).

In Fourier space, the coupled evolution equations are

$$\begin{aligned} \frac{\partial}{\partial t} \begin{pmatrix} \delta\bar{\phi}_q^{t\ m} \\ \delta\bar{\ell}_q^{t\ m} \end{pmatrix} &= -\underline{\underline{M}}(q) \cdot (\underline{\underline{C}}^m + q^2 \underline{\underline{P}}^m) \cdot \begin{pmatrix} \delta\bar{\phi}_q^{t\ m} \\ \delta\bar{\ell}_q^{t\ m} \end{pmatrix} \\ &\equiv -\underline{\underline{L}}^m(q) \cdot \begin{pmatrix} \delta\bar{\phi}_q^{t\ m} \\ \delta\bar{\ell}_q^{t\ m} \end{pmatrix}, \end{aligned} \quad (\text{B7})$$

where

$$\underline{\underline{M}}(q) \equiv \begin{pmatrix} Mq^2 & 0 \\ 0 & M\epsilon \end{pmatrix}. \quad (\text{B8})$$

The dimensionless parameter  $\epsilon \equiv \eta/M$  controls how ‘fast’ the thickness relaxation is relative to diffusion. Instabilities of the R or AR mode correspond to a negative eigenvalue of their  $\underline{\underline{L}}^m$ . Their wavenumber dependent growth rates are given by  $\omega^m(q) = -\lambda^m$  where  $\lambda^m$  is the eigenvalue for the eigenmode of  $\underline{\underline{L}}^m$ . Maximising  $\omega^m(q)$  over  $q$  yields  $\omega_{\max}^m$ , the peak growth rate of the given mode (R or AR).

The blue and red colours in Fig. 4 are obtained by first calculating  $\omega_{\max}^m$  for the R and AR modes. Then the difference  $\Delta\omega \equiv \omega_{\max}^R - \omega_{\max}^{\text{AR}}$  is plotted as the background of Fig. 4. If a given mode  $m$  has a negative peak growth rate (i.e. is not unstable) then its  $\omega_{\max}^m$  is set to zero. Thus  $\Delta\omega = 0$  (white) is ambiguous; either i) both modes are stable or ii) both are unstable but with equal peak growth rates. This ambiguity is easily resolved by referring to the instability lines when interpreting the plot, since if mode  $m$ ’s peak growth rate is zero then we must be outside the instability region of mode  $m$ . Note that the ranges of the colour scales in Fig. 4 are asymmetric.

To model the physically likely scenario we have used  $\epsilon = 100$ , since any frictional drag involved in stretching should be far less than that for lateral diffusion (23, 34). This value is close to ‘saturation’, i.e. the composition relaxation is the limiting timescale and significant further increases in  $\epsilon$  have only marginal quantitative effects on  $\omega^m(q)$ . Therefore the conclusions drawn from the colours in Fig. 4 are independent of  $\epsilon$  in the expected physical regime. Even if the opposite regime is assumed ( $\epsilon = 0.1$ ), the values of  $\omega^m(q)$  change but the key feature of the  $\Delta\omega$  landscape – which mode is fastest – is not strongly affected.

### Appendix C: Physical meaning of parameters

For comparison with phospholipids, we set the lattice spacing  $a \sim 0.8$  nm, corresponding to an area per lipid of  $0.64$  nm<sup>2</sup> (35).

#### 1. Stretching modulus

The stretching and compression of a bilayer of amphiphiles is measured experimentally via the area stretching modulus  $\kappa_A$ , with a free energy given by

$$G_{\kappa_A}^{\text{bilayer}} = \int d^2r \frac{\kappa_A}{2} \left( \frac{\delta A}{A_0} \right)^2, \quad (\text{C1})$$

where  $\delta A$  represents an area difference relative to the equilibrium area  $A_0$ . In the continuum representation of the lattice model here the stretching free energy for an individual leaflet of the bilayer is given by

$$G_\kappa^{\text{leaflet}} = \int \frac{d^2r}{a^2} \frac{\kappa}{2} (\delta\ell)^2, \quad (\text{C2})$$

where  $a^2$  is the lattice site area and  $\delta\ell$  is a tail length difference relative to an equilibrium length  $\ell_0$ . Assuming that the volume  $v = A\ell$  remains constant upon stretching/compression,  $A\delta\ell = -\ell\delta A$ , we have

$$G_\kappa^{\text{leaflet}} = \int d^2r \frac{\ell_0^2}{a^2} \frac{\kappa}{2} \left( \frac{\delta A}{A_0} \right)^2. \quad (\text{C3})$$

Noting that Eq. C1 describes the area stretching energy for the *whole* bilayer, and assuming the energy to be distributed evenly between the two leaflets, we can write

$$G_\kappa^{\text{leaflet}} = \frac{1}{2} G_{\kappa_A}^{\text{bilayer}}. \quad (\text{C4})$$

Identifying the lattice site area  $a^2$  as the equilibrium area per amphiphile  $A_0$  gives the correspondence

$$\kappa = \frac{A_0}{2\ell_0^2} \kappa_A, \quad (\text{C5})$$

where  $\ell_0$  is a representative value for the equilibrium length of a real amphiphile. For typical values  $\ell_0 = 2 \text{ nm}$  and  $A_0 = 0.64 \text{ nm}^2$  for phospholipid leaflets, the value  $\kappa = 3 a^{-2} k_B T$  used in this work corresponds to  $\kappa_A \approx 40 a^{-2} k_B T \approx 60 k_B T \text{ nm}^{-2}$ , in the range for lipid bilayers at 300 K (34, 36, 37).

## 2. Indirect coupling

The indirect coupling parameter  $\tilde{J}$  quantifies the penalty for mismatch in the total hydrophobic thickness between neighbouring lattice sites, arising from hydrophobic surface tension. We take a fiducial value  $\tilde{J} \approx 0.8 k_B T \text{ nm}^{-2}$ , approximately that estimated in Ref. (23) as a surface tension for hydrocarbon tails in contact with the watery headgroup region of phospholipids. This gives  $\tilde{J} \approx 0.5 a^{-2} k_B T$  for the lattice model, so for the mean-field parameter  $J \approx 2 a^{-2} k_B T$ . Increasing  $J$  (Fig. 4) can be thought of as increasing hydrophobic mismatch/hydrophobicity.

## 3. Direct coupling

The direct coupling parameter  $B$  plays a similar role to the inter-leaflet mismatch free energy  $\gamma$  estimated in the literature. We can define an effective  $\gamma$  (that shown in Fig. 4) by considering an isolated AR site and minimising its energy arising from stretching ( $\kappa$ ) and direct coupling ( $B$ ) energies over the top and bottom amphiphile lengths, where the reference state is an isolated R site which experiences zero direct coupling energy. This microscopic energy per AR site is

$$\gamma a^2 = \frac{\Delta_0^2 \kappa B}{2(\kappa + 2B)}, \quad (\text{C6})$$

in terms of which

$$B = \frac{2\gamma a^2 \kappa}{\kappa \Delta_0^2 - 4\gamma a^2}. \quad (\text{C7})$$

For example, the value  $\gamma \approx 0.15 k_B T \text{nm}^{-2}$  estimated in Ref. (22) is, in model units,  $\gamma \approx 0.1 a^{-2} k_B T$ . Assuming  $\Delta_0 = 1 a$  and  $\kappa = 3 a^{-2} k_B T$ , this gives  $B \approx 0.23 a^{-2} k_B T$ . In comparison to the other parameters, though,  $\gamma$  is poorly understood. Ref. (4) estimates an order of magnitude lower ( $\gamma \sim 0.01 a^{-2} k_B T$ , so that  $B \sim 0.02 a^{-2} k_B T$ ), and finds that the method used to extract  $\gamma$  in simulation (22) is inaccurate, since it assumes larger characteristic fluctuations than were measured. On the other hand, Ref. (21) finds that the effective  $\gamma$  measured while artificially pulling domains out of registration depends strongly on mismatch area, and proposes a role for membrane curvature, which we have not studied.

#### 4. Interpretation of $\gamma$

There are subtleties in defining the mismatch free energy per area  $\gamma$ . We have defined it ‘microscopically’ in Eq. C6 as the direct coupling energy density for an antiregistered site. It is possible instead to construct a ‘macroscopic’ definition by comparing the free energies of antiregistered and registered *domains*

$$\gamma_{\text{macro}} \equiv \lim_{A \rightarrow \infty} \frac{1}{A} (G^{\text{antireg}}(A) - G^{\text{reg}}(A)), \quad (\text{C8})$$

where  $G^{(\text{anti})\text{reg}}(A)$  is the free energy of an (anti)registered domain of area  $A$ . The limit  $A \rightarrow \infty$  emphasises that boundary contributions to the free energies are typically ignored (3, 4). For example, in Ref. (4),  $\gamma_{\text{macro}}$  is computed theoretically by comparing the free energies of antiregistered and registered arrangements of domains within a molecular mean-field theory, the domains being assumed large enough that contributions from their boundaries can be neglected. It is important to note that any effects of hydrophobic mismatch energy at the edges of registered domains (incorporated in our Ginzburg-Landau analysis via the  $\tilde{J}$  term of  $f_{\text{grad}}$ ) cannot be properly captured by  $\gamma$  or  $\gamma_{\text{macro}}$ , since these describe only energies that scale as the domain area.

In the well segregated limit such that an anti(registered) domain contains *purely* pairwise (anti)registered sites, the definition Eq. C8 becomes equivalent to Eq. C6. *Near* this limit, within our model  $\gamma_{\text{macro}} \approx \gamma$ , because the dominant contribution to the free energy difference in Eq. C8 will be from the direct coupling energy experienced by AR sites (Eq. C6), while contributions associated with the remnant fraction of pairwise R sites in the antiregistered demixed phase (and vice versa) will be small. Thus, for example, the free energy difference between the R and AR minima of  $f^{\text{[ann.]}}$  (Fig. 2) is similar to the value of  $\gamma$  quoted for that state point on Fig. 4e, calculated with Eq. C6.

In general, however, Eq. C8 requires specification of the compositions of the R and AR phases whose free energies are to be compared, and Fig. 3 shows us that the leaflet compositions in the AR phases generally differ from the those in the R phases. Therefore, the assumption (4) that the relevant AR configuration for comparison is that obtained by re-arranging the domains from the R configuration, *without altering their compositions*, is incorrect. It may be suitable for describing small fluctuations into AR at the boundary of a large R domain (as was the purpose in Ref. (4)), but only if one assumes that spatial fluctuations of the domain boundaries out of registration are not also accompanied by compositional fluctuations of the domains in each leaflet.

In some situations, even an approximate equality between  $\gamma$  and  $\gamma_{\text{macro}}$  breaks down due to ambiguity in implementing the macroscopic definition. Taking as given that R demixed phases exist in the free energy landscape, one might naturally assume that we should take the metastable AR phases in the free energy landscape for comparison. However, in Fig. 3 (top pane), R demixed minima exist but no metastable AR demixed minima exist – there is thus no thermodynamically (meta)stable AR phase to compare against the R phase in Eq. C8. In another case, in a small region of Fig. 4b the antiregistered phases are equilibrium. R demixed phases exist for comparison but are of *higher* free energy, which under Eq. C8 would imply a *negative* value of  $\gamma_{\text{macro}}$ , although the per-site  $\gamma$  defined by Eq. C6 is positive.

Hence, it is clear that describing inter-leaflet coupling is complex, both in terms of specifying the relevant bulk free energy and in terms of the domain size-dependent competition of edge and area energies. This latter aspect in particular, and its role in nucleation kinetics of domain registration, will be further studied in an upcoming publication. In relation to the present discussion, it is unclear precisely which coupling or combination of couplings is being measured in molecular simulation studies of inter-leaflet coupling (22), where the probability of fluctuations into antiregistration is monitored and fit to a Boltzmann distribution. These fluctuations may be subject to effects related to hydrophobic mismatch and composition dependence as discussed above, so that even if the approach of measuring fluctuations is essentially correct (challenged in Ref. (4)), it is likely that energies additional to that described by  $\gamma$  are at work. In summary, much further work is required in defining, measuring, and studying the implications of the competing forms of inter-leaflet coupling.

**Author contributions:** JJW designed the model, performed the research, and wrote the paper. PDO supervised the research and wrote the paper.

## ACKNOWLEDGMENTS

We acknowledge the EPSRC CAPITALS grant (EP/J017566/1) and discussions with A Aufderhorst-Roberts, HMG Barriga, NJ Brooks, P Cicuta, SD Connell, E Del Gado, SL Keller, H Kusumaatmaja, N McCarthy, D Rings and JM Seddon. This work was funded by EPSRC and Georgetown University. PDO gratefully acknowledges the support of the Ives endowment.

- 
1. Lingwood, D., and K. Simons, 2010. Lipid Rafts As a Membrane-Organizing Principle. *Science* 327:46–50.
  2. Kusumi, A., I. Koyama-Honda, and K. Suzuki, 2004. Molecular Dynamics and Interactions for Creation of Stimulation-Induced Stabilized Rafts from Small Unstable Steady-State Rafts. *Traffic* 5:213–230.
  3. May, S., 2009. Trans-monolayer coupling of fluid domains in lipid bilayers. *Soft Matter* 5:3148–3156.
  4. Garbès Putzel, G., M. J. Uline, I. Szleifer, and M. Schick, 2011. Interleaflet Coupling and Domain Registry in Phase-Separated Lipid Bilayers. *Biophys. J.* 100:996–1004.
  5. Funkhouser, C. M., M. Mayer, F. J. Solis, and K. Thornton, 2013. Effects of interleaflet coupling on the morphologies of multicomponent lipid bilayer membranes. *J. Chem. Phys.* 138:024909.

6. Allender, D., and M. Schick, 2006. Phase Separation in Bilayer Lipid Membranes: Effects on the Inner Leaf Due to Coupling to the Outer Leaf. *Biophys. J.* 91:2928–2935.
7. Garbès Putzel, G., and M. Schick, 2008. Phase Behavior of a Model Bilayer Membrane with Coupled Leaves. *Biophys. J.* 94:869–877.
8. Wagner, A. J., S. Loew, and S. May, 2007. Influence of Monolayer-Monolayer Coupling on the Phase Behavior of a Fluid Lipid Bilayer. *Biophys. J.* 93:4268–4277.
9. Hirose, Y., S. Komura, and D. Andelman, 2009. Coupled Modulated Bilayers: A Phenomenological Model. *ChemPhysChem* 10:2839–2846.
10. Korlach, J., P. Schwille, W. W. Webb, and G. W. Feigenson, 1999. Characterization of lipid bilayer phases by confocal microscopy and fluorescence correlation spectroscopy. *Proc. Natl. Acad. Sci.* 96:8461–8466.  
Dietrich, C., L. Bagatolli, Z. Volovyk, N. Thompson, M. Levi, K. Jacobson, and E. Gratton, 2001. Lipid Rafts Reconstituted in Model Membranes. *Biophys. J.* 80:1417–1428.  
Collins, M. D., and S. L. Keller, 2008. Tuning lipid mixtures to induce or suppress domain formation across leaflets of unsupported asymmetric bilayers. *Proc. Natl. Acad. Sci.* 105:124–128.
11. The mismatch free energy per area can be defined as  $\gamma \equiv (G^{\text{antireg}}(A) - G^{\text{reg}}(A))/A$ , where  $G^{\text{(anti)reg}}(A)$  is the free energy of a large (anti)registered domain of area  $A$ .
12. Zhang, J., B. Jing, N. Tokutake, and S. L. Regen, 2004. Transbilayer Complementarity of Phospholipids. A Look beyond the Fluid Mosaic Model. *J. Am. Chem. Soc.* 126:10856–10857.  
Zhang, J., B. Jing, V. Janout, and S. L. Regen, 2007. Detecting Cross Talk between Two Halves of a Phospholipid Bilayer. *Langmuir* 23:8709–8712.
13. Perlmutter, J. D., and J. N. Sachs, 2011. Interleaflet Interaction and Asymmetry in Phase Separated Lipid Bilayers: Molecular Dynamics Simulations. *J. Am. Chem. Soc.* 133:6563–6577.
14. Stevens, M. J., 2005. Complementary Matching in Domain Formation within Lipid Bilayers. *J. Am. Chem. Soc.* 127:15330–15331.  
Bennun, S. V., M. L. Longo, and R. Faller, 2007. Molecular-Scale Structure in Fluid-Gel Patterned Bilayers: Stability of Interfaces and Transmembrane Distribution. *Langmuir* 23:12465–12468.
15. Lin, W.-C., C. D. Blanchette, T. V. Ratto, and M. L. Longo, 2006. Lipid Asymmetry in DLPC/DSPC-Supported Lipid Bilayers: A Combined AFM and Fluorescence Microscopy Study. *Biophys. J.* 90:228 – 237.
16. Sornbundit, K., C. Modchang, W. Triampo, D. Triampo, N. Nuttavut, P. B. Sunil Kumar, and M. Laradji, 2014. Kinetics of domain registration in multicomponent lipid bilayer membranes. *Soft Matter* 10:7306–7315.
17. Hydrophobic mismatch appears naturally in more complex molecular models (38). It was included in coarse-grained modelling in (23), but without resolving the individual leaflets.
18. Komura, S., H. Shirotori, P. D. Olmsted, and D. Andelman, 2004. Lateral phase separation in mixtures of lipids and cholesterol. *Europhys. Lett.* 67:321.
19. Bagatolli, L., and P. B. Sunil Kumar, 2009. Phase behavior of multicomponent membranes: Experimental and computational techniques. *Soft Matter* 5:3234–3248.
20. Honerkamp-Smith, A. R., P. Cicuta, M. D. Collins, S. L. Veatch, M. den Nijs, M. Schick, and S. L. Keller, 2008. Line Tensions, Correlation Lengths, and Critical Exponents in Lipid Membranes Near Critical Points. *Biophys. J.* 95:236–246.
21. Pantano, D. A., P. B. Moore, M. L. Klein, and D. E. Discher, 2011. Raft registration across bilayers in a molecularly detailed model. *Soft Matter* 7:8182–8191.

22. Risselada, H. J., and S. J. Marrink, 2008. The molecular face of lipid rafts in model membranes. *Proc. Natl. Acad. Sci.* 105:17367–17372.
- Polley, A., S. Mayor, and M. Rao, 2014. Bilayer registry in a multicomponent asymmetric membrane: Dependence on lipid composition and chain length. *J. Chem. Phys.* 141:064903.
23. Wallace, E. J., N. M. Hooper, and P. D. Olmsted, 2006. Effect of Hydrophobic Mismatch on Phase Behavior of Lipid Membranes. *Biophys. J.* 90:4104–4118.
24. Poon, W. C. K., F. Renth, R. M. L. Evans, D. J. Fairhurst, M. E. Cates, and P. N. Pusey, 1999. Colloid-Polymer Mixtures at Triple Coexistence: Kinetic Maps from Free-Energy Landscapes. *Phys. Rev. Lett.* 83:1239–1242.
25. While laterally mixed, the bilayer can contain more or fewer *pairwise* R vs. AR sites. At  $\bar{\phi}^b = \bar{\phi}^t = 0.5$  in particular, anything from full pairwise R to AR is possible.
26. In principle the mixed state may become metastable against AR demixing if  $B \gg J$ , but for phospholipids the literature suggests  $J \gtrsim B$  or  $J \gg B$  (see Appendix C). Further, the ‘complementary matching’ (pairwise AR) measured in (12) requires, within our model,  $J > B$  (via Eq. 8).
27. Chaikin, P., and T. Lubensky, 2000. Principles of Condensed Matter Physics. Cambridge University Press.
28. The possible nucleation kinetics involved will be studied in an upcoming publication.
29. Lee, J. S., and J. Feijen, 2012. Polymersomes for drug delivery: Design, formation and characterization. *J. Control. Release* 161:473 – 483.
30. Schulz, M., D. Glatte, A. Meister, P. Scholtysek, A. Kerth, A. Blume, K. Bacia, and W. H. Binder, 2011. Hybrid lipid/polymer giant unilamellar vesicles: effects of incorporated biocompatible PIB-PEO block copolymers on vesicle properties. *Soft Matter* 7:8100–8110.
31. Brewster, R., P. Pincus, and S. Safran, 2009. Hybrid Lipids as a Biological Surface-Active Component. *Biophys. J.* 97:1087–1094.
32. Shlomovitz, R., and M. Schick, 2013. Model of a Raft in Both Leaves of an Asymmetric Lipid Bilayer. *Biophys. J.* 105:1406–1413.
33. Goldenfeld, N., 1992. Lectures on Phase Transitions and the Renormalization Group. Addison-Wesley, New York.
34. Wallace, E. J., 2005. Influence of microstructure on the phase behaviour of lipid membranes. Ph.D. thesis, University of Leeds.
35. Kučerka, N., M.-P. Nieh, and J. Katsaras, 2011. Fluid phase lipid areas and bilayer thicknesses of commonly used phosphatidylcholines as a function of temperature. *Biochim. Biophys. Acta* 1808:2761 – 2771.
36. Needham, D., and R. Nunn, 1990. Elastic deformation and failure of lipid bilayer membranes containing cholesterol. *Biophys. J.* 58:997 – 1009.
37. Rawicz, W., K. Olbrich, T. McIntosh, D. Needham, and E. Evans, 2000. Effect of Chain Length and Unsaturation on Elasticity of Lipid Bilayers. *Biophys. J.* 79:328 – 339.
38. Longo, G. S., M. Schick, and I. Szleifer, 2009. Stability and Liquid-Liquid Phase Separation in Mixed Saturated Lipid Bilayers. *Biophys. J.* 96:3977 – 3986.